



Diurnal evolution of synergistic interactions between urban heat islands and heat waves: An extreme heat wave case study in Seoul, South Korea

Kyeongjoo Park, Jong-Jin Baik ^{*}

School of Earth and Environmental Sciences, Seoul National University, Seoul 08826, South Korea

ARTICLE INFO

Keywords:

Urban heat island
Heat wave
Synergistic interactions
Diurnal evolution
Thermodynamic energy budget
Seoul

ABSTRACT

The synergistic interactions between urban heat islands (UHIs) and heat waves (HWs) refer to a phenomenon that UHIs are intensified during HWs, resulting in a greater temperature increase due to HWs in urban areas than in rural areas. Despite significant variations of the UHI–HW synergies on a diurnal timescale, their key physical processes are still not clearly understood. This study examines the diurnal evolution of the UHI–HW synergies and its underlying physical processes. For this, we simulate an extreme HW event with strong UHI–HW synergies in Seoul, South Korea using the Weather Research and Forecasting (WRF) model. The UHI–HW synergies rapidly strengthen in early evening and diminish in early morning, similar to the diurnal pattern found in many large cities. In early evening, the rural diabatic cooling is greatly enhanced under clearer skies during HW while the increases in both urban stored heat release and urban turbulent mixing result in only a slight change in urban diabatic heating. These contrasting responses are primarily responsible for the strengthening of the UHI–HW synergies. In early morning, the warm air advection from the rural residual layer by subsidence significantly increases under HW while subsidence rarely occurs in the urban boundary layer. These different responses to HW are mainly responsible for the weakening of the UHI–HW synergies. This study underlines the importance of differing changes in urban and rural near-surface thermodynamic processes during HWs on the temporal evolution of the UHI–HW synergies.

1. Introduction

Urban residents experience increasing heat risks with continuing global warming and urbanization (Tuholske et al., 2021). Heat waves (HWs), sustained periods of abnormally hot weather, have become more frequent in numerous cities across the globe (Mishra et al., 2015). Urban heat islands (UHIs), a phenomenon characterized by higher temperatures in urban areas than in their surrounding rural areas, have also become stronger in over 60 % of cities worldwide (Yang et al., 2024). In the future, urban heat risks driven by HWs and UHIs are projected to rapidly increase (Huang et al., 2019; Marcotullio et al., 2022), necessitating effective adaptation and mitigation strategies to reduce heat-related health problems (Fu et al., 2024; Cuce et al., 2025).

HWs are usually caused by persistent synoptic high-pressure systems (Barriopedro et al., 2023), occurring in both urban areas and their surrounding areas. On the other hand, UHIs primarily result from different surface characteristics in urban areas compared to rural areas (Deilami et al., 2018) and therefore occur within urban areas. Due to the presence of UHIs, heat risks during HWs are greater in urban areas than in rural

areas (Basara et al., 2010; Guindon and Nirupama, 2015). Moreover, UHIs and HWs can synergistically interact with each other, further exacerbating urban heat risks (Li and Bou-Zeid, 2013). The synergistic interactions between UHIs and HWs (UHI–HW synergies) refer to a phenomenon that UHIs become stronger during HWs than during non-HWs (Kong et al., 2021). The magnitude of the UHI–HW synergies, denoted by ΔT_{syn} , is expressed as:

$$\Delta T_{\text{syn}} = (T_{u,\text{HW}} - T_{r,\text{HW}}) - (T_{u,\text{non-HW}} - T_{r,\text{non-HW}}) \quad (1)$$

where $T_{u,\text{HW}}$ and $T_{r,\text{HW}}$ are, respectively, the urban and rural temperatures during HWs and $T_{u,\text{non-HW}}$ and $T_{r,\text{non-HW}}$ are, respectively, the urban and rural temperatures during non-HWs. Alternatively, ΔT_{syn} can be expressed as:

$$\Delta T_{\text{syn}} = (T_{u,\text{HW}} - T_{u,\text{non-HW}}) - (T_{r,\text{HW}} - T_{r,\text{non-HW}}) \quad (2)$$

thus, ΔT_{syn} also represents how much additional warming occurs in urban areas during HWs compared to rural areas, quantifying how urban and rural temperatures respond differently to HWs. In this study, we

* Corresponding author.

E-mail address: jjaik@snu.ac.kr (J.-J. Baik).

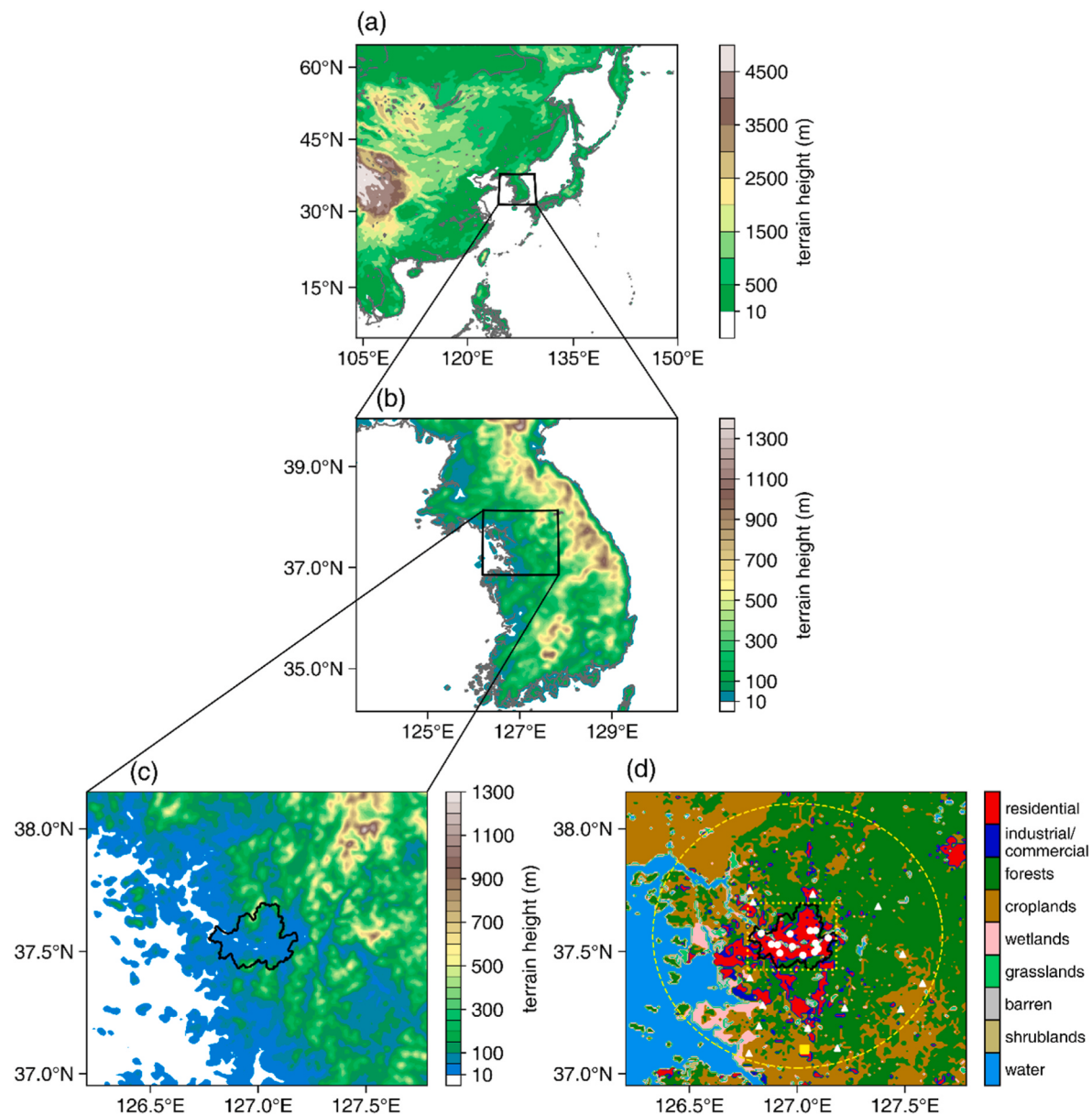


Fig. 1. (a) Outermost domain, (b) intermediate domain, and (c) innermost domain with terrain height (shaded). (d) Innermost domain with land use types. The analysis area is indicated by the yellow dashed circle. The administrative boundary of Seoul is indicated by the thick black solid line in (c) and (d). The area surrounding the administrative boundary of Seoul is indicated by the yellow dotted rectangle in (d). The white dots (triangles) in (d) denote the weather stations inside (outside) Seoul used for model validation. The yellow square in (d) denotes the radiosonde station used for model validation.

examine and discuss the UHI–HW synergies occurring near the surface which directly affect thermal discomfort. Previous studies revealed that the UHI–HW synergies occur during HWs in numerous cities under various background climates (Zhao et al., 2018; Pyrgou et al., 2020; Zong et al., 2021; Possega et al., 2022; Luo et al., 2023; Syed Mahbar and Kusaka, 2024). Zhao et al. (2018) showed that in 15 cities in the U.S. with dry climates, ΔT_{syn} is on average 0.4 °C during the nighttime in 1975–2004. Luo et al. (2023) showed that in Guangzhou, China with a subtropical climate, ΔT_{syn} is overall ~0.9 °C in 2013–2018. Syed Mahbar and Kusaka (2024) found that in Greater Kuala Lumpur, Malaysia with a tropical climate, ΔT_{syn} reaches 2.3 °C during an extreme HW event in 2016.

From the diurnal patterns of ΔT_{syn} shown in previous studies, it can be found that ΔT_{syn} in many large cities strengthen in early evening while they diminish in early morning, exhibiting their greater magnitudes during the nighttime than during the daytime (Ramamurthy et al., 2017; Jiang et al., 2019; An et al., 2020; Park et al., 2023; Ma et al.,

2024; Syed Mahbar and Kusaka, 2024). For instance, in New York City, U.S. and Beijing, China, the diurnal patterns of ΔT_{syn} with a sharp increase around ~1800 LST and a sharp decrease around ~0600 LST are observed (Ramamurthy et al., 2017; Jiang et al., 2019; An et al., 2020). Similar characteristics are also observed in Seoul, South Korea (Park et al., 2023). Despite significant variations of ΔT_{syn} on a diurnal time-scale, the underlying physical processes are still not well understood. Previous studies investigated how urban and rural surface energy fluxes change in different ways during HWs to identify key factors affecting daytime and/or nighttime UHI–HW synergies (Li et al., 2015; Zhao et al., 2018; Ao et al., 2019; He et al., 2020; Cui et al., 2023). However, due to the presence of various thermodynamic processes occurring in near-surface atmosphere such as advection, turbulent mixing, and microphysical processes in addition to heating/cooling related to surface energy fluxes (Kim et al., 2024b; Park et al., 2024), the UHI–HW synergies occurring near the surface and their diurnal evolution are hard to be fully elucidated by changes in surface energy fluxes due to HWs

alone. Given that the near-surface temperature and its temporal evolution are directly governed by near-surface thermodynamic energy budgets, analyzing how urban and rural near-surface thermodynamic energy budgets alter differently during HWs could lead to a better understanding of the diurnal evolution of the UHI–HW synergies occurring near the surface and its associated key physical processes.

This study aims to examine the diurnal evolution of the UHI–HW synergies and its underlying physical processes in detail. For this, we conduct a numerical simulation of an extreme HW event occurring in Seoul and its surrounding areas, during which strong UHI–HW synergies appear, and perform a detailed analysis of HW-induced changes in urban and rural near-surface thermodynamic energy budgets. Seoul is the most heavily urbanized area in South Korea, with a population density of 15506 people km^{-2} in 2023 (<https://kosis.kr>). Seoul (37.41–37.72°N, 126.73–127.27°E) falls within the humid continental climate (Dwa), experiencing hot and humid summers and cold and dry winters (Beck et al., 2018). Recently, pronounced UHI–HW synergies have frequently occurred in Seoul (Park et al., 2023), requiring a thorough examination of this phenomenon in Seoul. In Section 2, the simulation setup and analysis method are described. In Section 3, the description of the analyzed HW event, model validation, and the analysis of the UHI–HW synergies and their associated key physical processes are presented. Section 4 provides the summary and conclusions of this study.

2. Method

2.1. Numerical model and simulation setup

To examine the diurnal evolution of the UHI–HW synergies and its associated physical processes, a numerical simulation is conducted using the Weather Research and Forecasting (WRF) model version 4.1.3 (Skamarock et al., 2019). Fig. 1 presents the three model domains with the two-way nesting option employed for the simulation. The innermost domain covers Seoul and its surrounding areas (Fig. 1c). The number of grid points (horizontal grid resolution) is 250 × 250 (25 km), 130 × 130 (5 km), and 145 × 135 (1 km) in the outermost, intermediate, and innermost domains, respectively. All three domains consist of 70 vertical layers in which the lowest model level is ~43 m and the model-top pressure is 20 hPa. Following Ryu and Baik (2013), the Shuttle Radar Topography Mission (SRTM) data (Farr et al., 2007) with a horizontal resolution of ~90 m are used for topography and the land use/land cover data with a resolution of 4 m, generated by the Korea Ministry of Environment (<https://egis.me.go.kr>), are used.

To parameterize physical processes, the Dudhia shortwave radiation scheme (Dudhia, 1989), the Rapid Radiative Transfer Model (RRTM) longwave radiation scheme (Mlawer et al., 1997), the WRF single-moment 6-class microphysics scheme (Hong and Lim, 2006), the Kain–Fritsch convection scheme (Kain, 2004), the Yonsei University planetary boundary layer (PBL) scheme (Hong et al., 2006), the revised MM5 surface layer scheme (Jiménez et al., 2012), the unified Noah land surface model (Chen and Dudhia, 2001), and the Seoul National University urban canopy model (SNUUCM) (Ryu et al., 2011) are used. The SNUUCM realistically represents urban surface physical processes (Ryu et al., 2011) and satisfactorily simulates urban surface energy fluxes (Lipson et al., 2024). Following Baik et al. (2022), the mean building height is set to 22.5 and 30 m for residential and industrial/commercial areas, respectively. Other urban-parameter values are set to the same values as those in Chen et al. (2011). For anthropogenic heat, the gridded dataset of anthropogenic heat flux over South Korea, estimated by Lee and Kim (2015) with a 1-km horizontal resolution, is used. Note that the convection scheme is turned off in the innermost domain.

To provide initial and boundary conditions, the fifth-generation European Centre for Medium-Range Weather Forecasts (ECMWF) reanalysis (ERA5) data (0.25° × 0.25°, 1-h resolutions) (Hersbach et al., 2020) are used. The simulation period extends from 0000 LST July 4, 2021 to 0000 LST August 18, 2021 (45 days). The first 24-h period

extending from 0000 LST July 4, 2021 to 0000 LST July 5, 2021 is considered as a spin-up period. The time step is 30 s in the outermost domain, 6 s in the intermediate domain, and 1.2 s in the innermost domain. To ensure an accurate 45-day simulation, the analysis nudging is applied to temperature, horizontal wind velocities, and water vapor mixing ratio above the PBL using the ERA5 data. The nudging coefficients used for temperature, horizontal wind velocities, and water vapor mixing ratio are 0.0003, 0.0003, and 0.00001 s^{-1} , respectively. The nudging interval is set to 1 h.

2.2. Analysis method

In this study, all major analyses are performed within the analysis area of a 60-km radius from the center of Seoul in the innermost domain (yellow dashed circle in Fig. 1d). The urban 2-m temperature is calculated as the average 2-m temperature over the urban grids in the rectangular area surrounding Seoul (yellow dotted rectangle in Fig. 1d). Meanwhile, the rural 2-m temperature is calculated as the average 2-m temperature over the non-urban grids in the analysis area excluding the rectangular area. The UHI intensity is calculated as the difference between the urban 2-m temperature and rural 2-m temperature (former minus latter). To assess changes in UHI intensity under HW (21–31 July) compared to that during non-HW periods, a pre-HW period from 5 July to 11 July and a post-HW period from 11 August to 17 August are considered as non-HW. In analysis, 1200–1700 LST is classified as daytime and 0000–0500 LST is classified as nighttime.

To examine physical processes primarily responsible for the diurnal evolution of the UHI–HW synergies, changes in urban and rural near-surface thermodynamic energy budgets under HW compared to non-HW are investigated. In height coordinates, the thermodynamic energy equation is expressed as follows:

$$\frac{\partial T}{\partial t} = -u \frac{\partial T}{\partial x} - v \frac{\partial T}{\partial y} - w \frac{\partial T}{\partial z} + \omega \frac{\alpha}{c_p} + \frac{Q}{c_p} \quad (3)$$

here, T is the air temperature, u , v , and w are, respectively, the wind velocities in the x -direction, y -direction, and z -direction, ω is the vertical pressure velocity, α is the specific volume of air, c_p is the specific heat of dry air at constant pressure (1004 $\text{J kg}^{-1} \text{K}^{-1}$), and Q is the diabatic heating/cooling rate. In Eq. (3), $\partial T/\partial t$ is the local temperature tendency and $-u\partial T/\partial x - v\partial T/\partial y$, $-w\partial T/\partial z$, $\omega\alpha/c_p$, and Q/c_p are the temperature tendencies due to horizontal advection, vertical advection, adiabatic heating/cooling, and diabatic heating/cooling, respectively. Upon Eq. (3), we attribute the local tendency of simulated 2-m temperature ($\partial T/\partial t$) to horizontal advection ($-u\partial T/\partial x - v\partial T/\partial y$), vertical advection ($-w\partial T/\partial z$), adiabatic heating/cooling ($\omega\alpha/c_p$), and diabatic heating/cooling (Q/c_p). This is to interpret the differences in change in 2-m temperature evolution due to HWs between the urban and rural areas upon the thermodynamic energy equation. The advections and adiabatic heating/cooling are quantified based on the fields of 2-m temperature, 2-m wind, and surface pressure and their temporal changes. We calculate the 2-m horizontal wind velocities using the Monin–Obukhov similarity theory, the formulation being consistent with that provided in Jiménez et al. (2012). The 2-m vertical wind velocity is calculated using the mass continuity equation. Note that the main results of the budget analysis are robust regardless of whether the 2-m or 10-m wind velocities are used. For the calculation of the vertical advection term ($-w\partial T/\partial z$), the temperature at the lowest model level (~43 m) is additionally used. For the calculation of the adiabatic heating/cooling term ($\omega\alpha/c_p$), α is calculated using the ideal gas law and ω is calculated as the material derivative of the surface pressure. The remaining local tendency of the 2-m temperature not attributed to the advections and adiabatic heating/cooling is attributed to the diabatic heating/cooling by all physical processes (Q/c_p). This residual approach to quantify the diabatic heating/cooling term in the thermodynamic energy equation was also adopted in previous modeling and reanalysis-based studies (e.g.

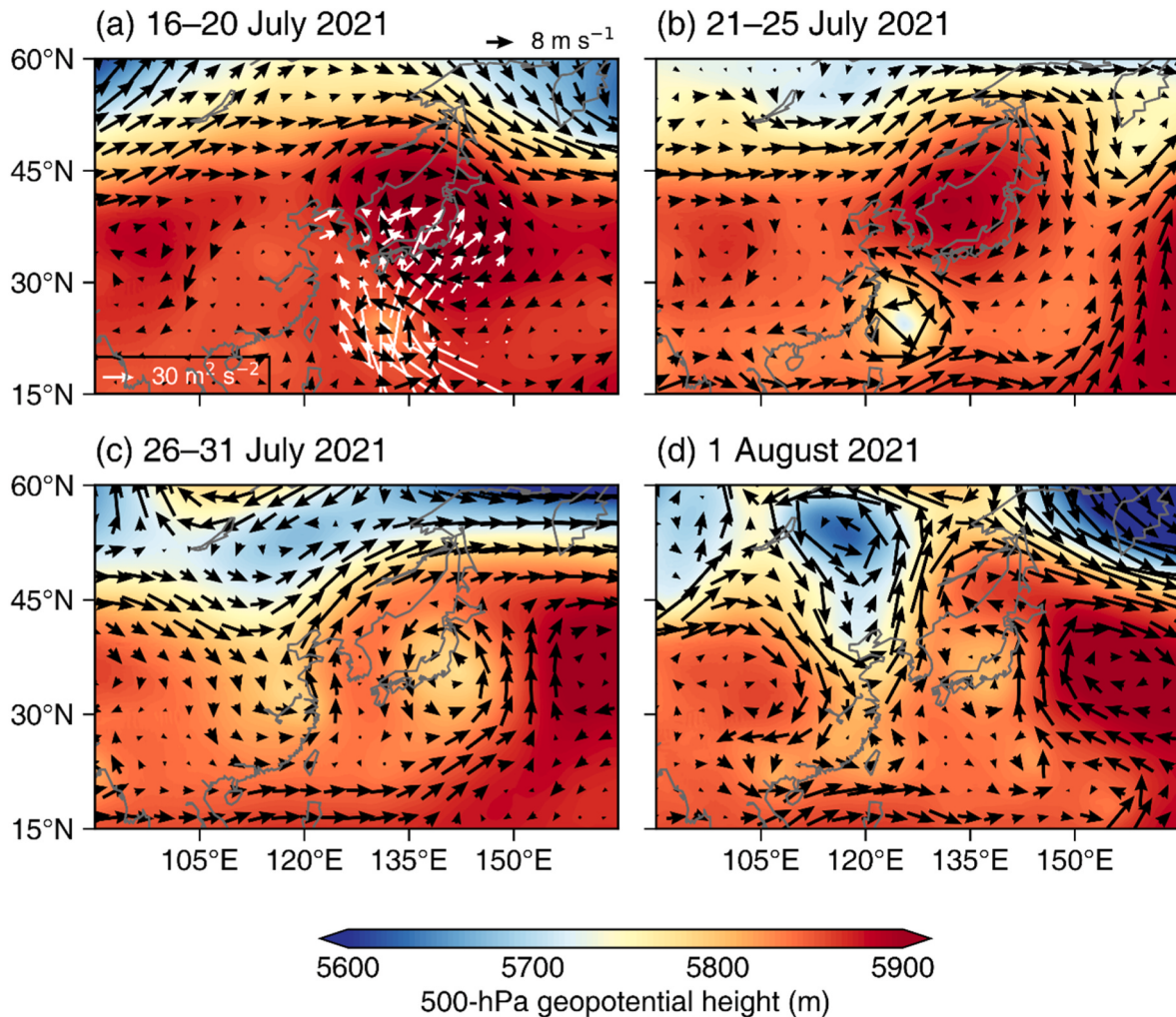


Fig. 2. Fields of geopotential height and horizontal wind vector at the 500-hPa level during (a) 16–20 July, (b) 21–25 July, (c) 26–31 July, and (d) 1 August 2021. The wave activity flux at the 850-hPa level and over the 20–40°N and 125–150°E area is indicated by the white arrow in (a).

g., Chan and Nigam, 2009; Martins et al., 2016; Gao et al., 2025). Individual terms in Eq. (3) are calculated for each grid, and then they are spatially averaged in the same way as the calculations of the urban 2-m temperature and rural 2-m temperature to obtain the representative tendencies for the urban and rural areas, respectively.

Finally, how the HW-induced changes in individual energy budget terms are different between the urban and rural areas is investigated:

$$\Delta \left(\frac{\partial T}{\partial t} \right) = \Delta \left(-u \frac{\partial T}{\partial x} - v \frac{\partial T}{\partial y} \right) + \Delta \left(-w \frac{\partial T}{\partial z} \right) + \Delta \left(\frac{\omega \alpha}{c_p} \right) + \Delta \left(\frac{Q}{c_p} \right) \quad (4)$$

here, Δ means the difference between HW and non-HW (HW minus non-HW). This study adopts a different approach from Park et al. (2024) in which the thermodynamic energy budget in the first model layer is analyzed using the WRF model and the temperature tendency due to diabatic processes is further decomposed into those by radiation, PBL processes, and microphysical processes. This is because in this study, the lowest-model-level height is set to be quite distant (~ 43 m) from the near-surface level due to the mean building heights set in the simulation (22.5 m, 30 m), the lowest-model-level temperature being less representative of near-surface thermal environment than the 2-m temperature.

3. Results and discussion

3.1. Case description

From 21 to 31 July in 2021, an extreme HW occurred in Seoul and its surrounding areas. In Seoul, this event is characterized by the fourth longest duration and the ninth strongest maximum intensity since 1973 (<https://data.kma.go.kr>). During the HW event, the highest 2-m temperature in Seoul reached 39.2 °C and the mean daily maximum 2-m temperature was 36.7 °C. The mean daily relative humidity and cloud fraction were, respectively, 62.5 % and 4.4 (in tenth), representing statistically significantly ($p < 0.05$) drier and clearer weather conditions compared to the 25-year climatological mean. Under these weather conditions favorable for the intensification of UHIs, the strongest UHI intensity quantified using weather stations employed in Park et al. (2023) reached 5.02 °C, the UHI–HW synergies being pronounced. On the other hand, the mean daily maximum 2-m temperature and mean daily relative humidity and cloud fraction under non-HW in Seoul were, respectively, 31.0 °C, 72.6 %, and 6.7, overall without anomalous weather conditions compared to the climatological mean.

The synoptic characteristics of the HW event are analyzed using the ERA5 data. Fig. 2 shows the 500-hPa geopotential height and horizontal wind vector fields before, during, and after the HW event. The mean 850-hPa wave activity fluxes (Takaya and Nakamura, 2001) over the 20–40°N and 125–150°E area during the 5-day period (16–20 July)

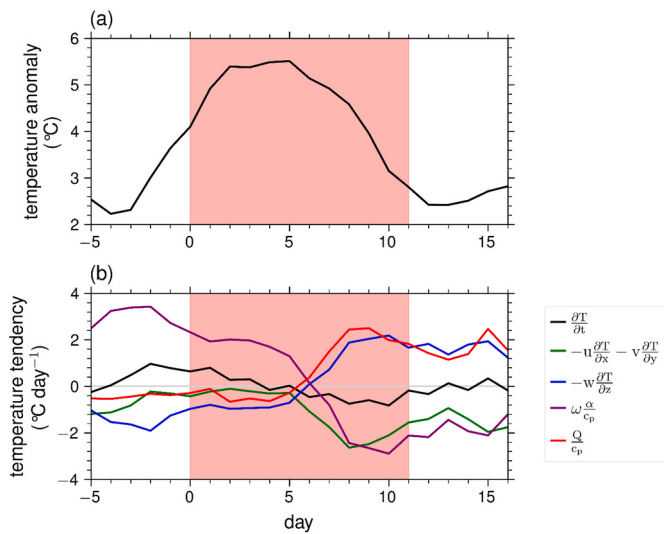


Fig. 3. (a) Time series of 5-day running-averaged daily mean temperature anomaly at the 1000-hPa level from 5 days before to 16 days after the onset of the heat wave event. The light red shaded area denotes the heat wave event. (b) Same as (a) except for local temperature tendency (black) and the temperature tendencies due to horizontal advection (green), vertical advection (blue), adiabatic processes (purple), and diabatic processes (red) at the 1000-hPa level.

before the HW event are also shown in Fig. 2a. During 16–20 July, the western North Pacific subtropical high (WNPSH) expands to the Korean Peninsula while a distinct low, typhoon In-Fa, is found over the Philippine Sea (Fig. 2a). It is clearly seen that the wave activity fluxes are directed from typhoon In-Fa to the regions where the WNPSH expands, suggesting that the enhanced convective activities due to the typhoon

trigger a Rossby wave train toward the north/northeast and contribute to the northwestward expansion of the WNPSH (Matsumura et al., 2015; Kubota et al., 2016; Hu et al., 2023; Tseng and Ho, 2024). The atmospheric teleconnection linking the tropical western North Pacific to East Asia via a Rossby wave train is known as the Pacific–Japan pattern (Nitta, 1987; Kosaka and Nakamura, 2006) and is significantly associated with the occurrence of HWs in South Korea (Noh et al., 2021; Kim et al., 2024c). During 21–25 July, a portion of the expanded WNPSH detaches and forms an isolated high-pressure system (Fig. 2b). A strong subsidence occurs under the high-pressure system, the mean 850-hPa vertical pressure velocity over the Korean Peninsula being 0.03 Pa s^{-1} . During 26–31 July, the high-pressure system over the Korean Peninsula weakens and is located between a trough over China and a cyclonic low over Japan (Fig. 2c). On 1 August, the Korean Peninsula is influenced by a well-developed trough over the northwest of the Korean Peninsula in the mid-to-upper levels (Fig. 2d). On this day, precipitation occurs throughout Seoul and its surrounding areas with a maximum daily precipitation of 21.0 mm, leading the HW event to end.

The physical processes mainly responsible for regional/local warming during the HW event are examined upon the thermodynamic energy equation (Eq. (3)). Here, the 1000-hPa temperature, horizontal wind velocities, and vertical pressure velocity from the ERA5 data are used. For the calculation of the vertical advection term ($-w\partial T/\partial z$), the 950-hPa level temperature is additionally used. α in the adiabatic heating/cooling term is calculated in the same way as that described in subsection 2.2. Fig. 3a shows the 5-day running averaged 1000-hPa temperature anomaly from its climatological (1992–2021) mean at the grid point ($37.5^\circ\text{N}, 127.0^\circ\text{E}$) within Seoul from 5 days before to 16 days after the onset of the HW event. The daily variation of the 1000-hPa temperature anomaly during this period is highly similar to that of observed daily mean 2-m temperature in Seoul (Supplementary Material Fig. S1), with a correlation coefficient (R) of 0.98. Throughout the period, the

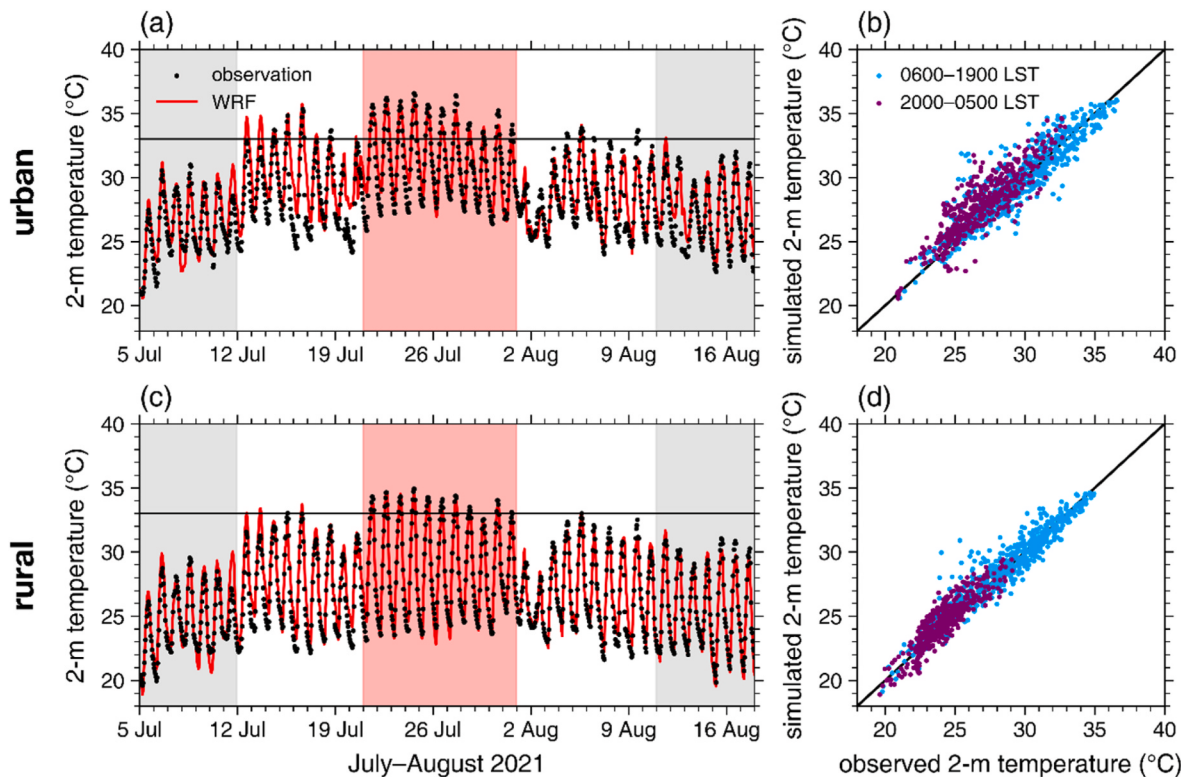


Fig. 4. (a) Time series of observed (black dots) and simulated (red solid line) 2-m temperatures averaged over the locations of urban stations. The black horizontal line denotes 33°C . The shaded areas denote HW (light red) and non-HW (light gray). (b) Scatterplot of observed versus simulated 2-m temperature averaged over the locations of urban stations during 0600–1900 LST (sky-blue) and 2000–0500 LST (purple). (c) Same as (a) except for the locations of rural stations. (d) Same as (b) except for the locations of rural stations.

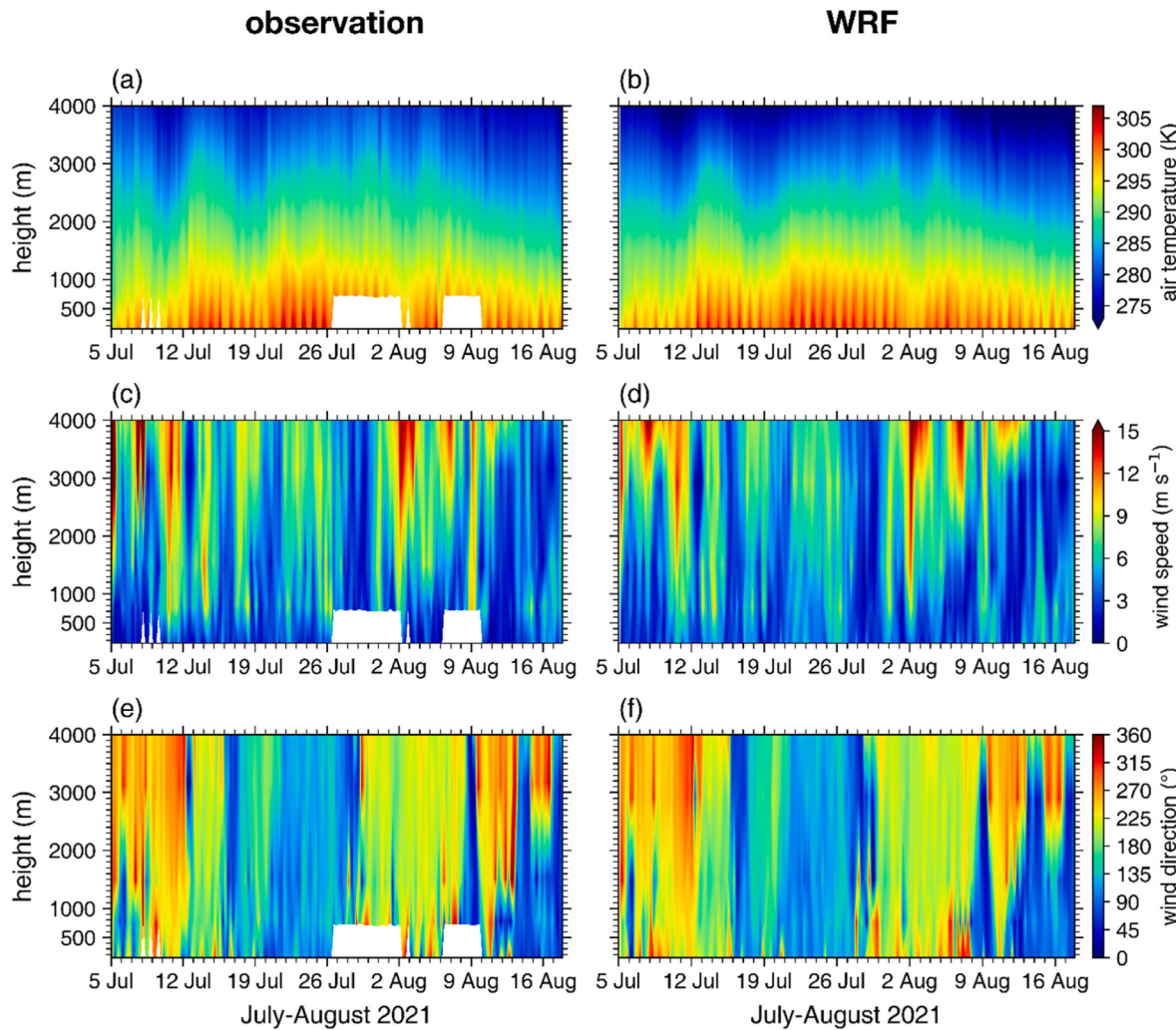


Fig. 5. Time-height cross sections of air temperatures (a) observed at the radiosonde station and (b) simulated by the WRF model during the analysis period. Time-height cross sections of wind speeds (c) observed at the radiosonde station and (d) simulated by the WRF model during the analysis period. Time-height cross sections of wind directions (e) observed at the radiosonde station and (f) simulated by the WRF model during the analysis period. The white areas in (a), (c), and (e) denote the missing values.

1000-hPa temperature anomaly remains above 2.00 °C, indicating significantly warmer conditions than the climatological mean (Fig. 3a). From −4 day to +5 day, the 1000-hPa temperature anomaly increases by 3.28 °C, the peak value being 5.51 °C. The 1000-hPa temperature anomaly decreases from 5.51 °C to 2.80 °C from +5 day to +11 day and slightly varies after the HW event.

Fig. 3b is the same as Fig. 3a except for $\partial T/\partial t$, $-u\partial T/\partial x-v\partial T/\partial y$, $-w\partial T/\partial z$, $\omega\alpha/c_p$, and Q/c_p at the 1000-hPa level. The largest positive temperature tendency from −4 day to +5 day is found for $\omega\alpha/c_p$, the adiabatic heating primarily contributing to the overall positive $\partial T/\partial t$ during this period (Fig. 3b). The mean $\omega\alpha/c_p$ from −4 day to +5 day is $2.31 \text{ }^{\circ}\text{C day}^{-1}$. The horizontal advection results in negative temperature tendencies throughout the period from −5 day to +16 day. The vertical advection and diabatic processes generally bring about temperature tendencies opposite to those resulting from adiabatic processes, reducing the magnitude of $\partial T/\partial t$. As $\omega\alpha/c_p$ becomes negative and $-u\partial T/\partial x-v\partial T/\partial y$ decreases after +5 day, $\partial T/\partial t$ also becomes negative from +5 day to +11 day. Thus, it is concluded that the adiabatic heating by subsidence plays the most crucial role in elevating regional/local temperature during the HW event. The adiabatic heating was also found to be the key physical process associated with the record-breaking HW in South Korea in 2018 (Kim et al., 2024c).

3.2. Model validation

The WRF model is validated using 2-m temperatures observed at 13 weather stations (urban stations) in Seoul and 14 weather stations (rural stations) around Seoul (Park et al., 2023) as well as air temperature and wind profiles observed at Osan radiosonde station (37.10°N, 127.03°E) (Fig. 1d). The simulated 2-m temperatures at the locations of urban and rural stations are compared with observations in Fig. 4. The 2-m temperatures at the locations of both urban and rural stations are accurately simulated in the WRF model (Fig. 4a and c), with R of 0.92 and 0.96 and the root mean square errors (RMSEs) of 1.37 and 0.95 °C, respectively. Moreover, the simulated 2-m temperatures at the locations of urban and rural stations exhibit quite low biases during both daytime and nighttime (Fig. 4b and d), the diurnal variations of 2-m temperature being well reproduced in the urban and rural areas. The mean bias error (MBE) of simulated 2-m temperatures averaged over the locations of urban (rural) stations is 0.90 °C (0.32 °C) during 0600–1900 LST and is 0.17 °C (0.20 °C) during 2000–0500 LST.

Fig. 5 shows the time-height cross sections of observed and simulated air temperatures, wind speeds, and wind directions at the location of the radiosonde station. For comparisons, an interpolation is performed to obtain the simulated air temperature, wind speed, and wind direction at observed heights. The WRF model tends to underestimate air

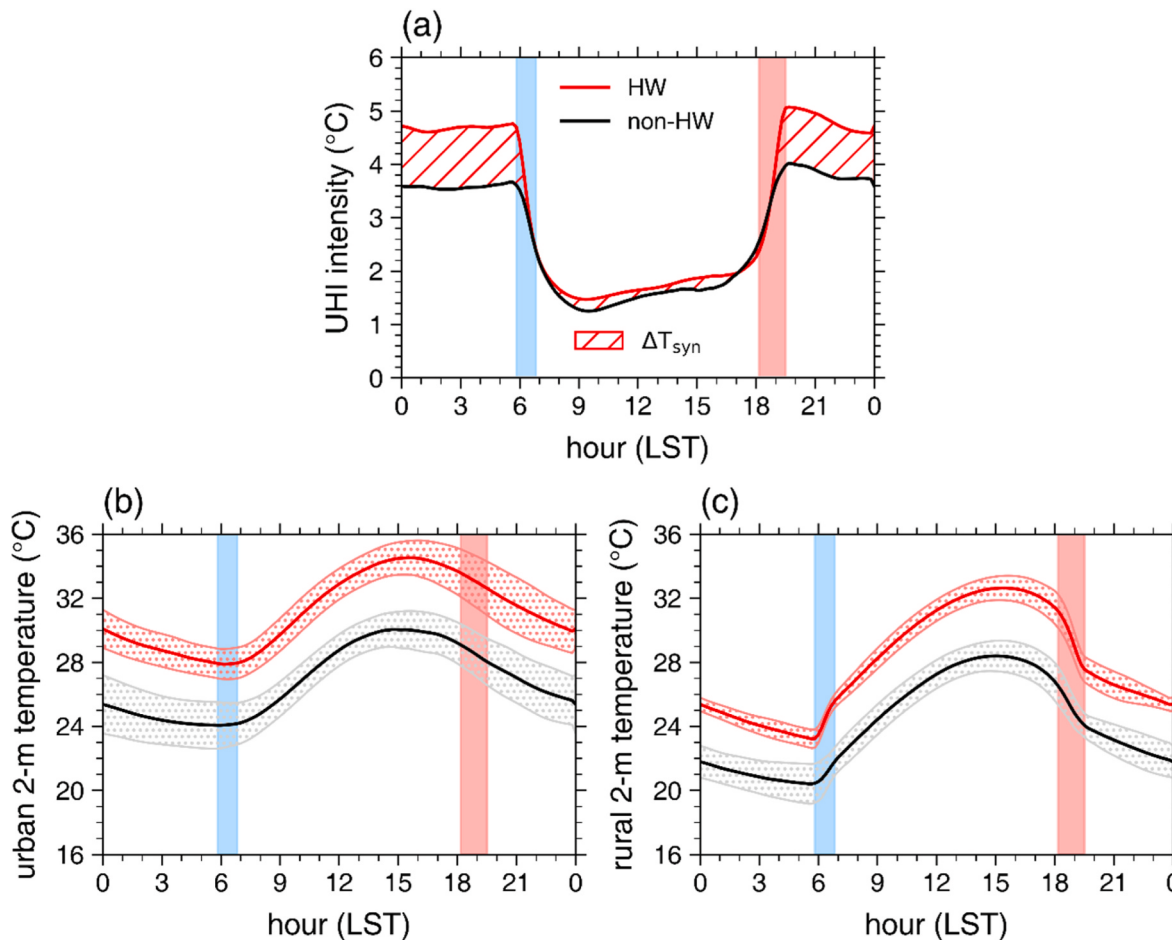


Fig. 6. Diurnal variations of (a) urban heat island intensities, (b) urban 2-m temperatures, and (c) rural 2-m temperatures under HW (red) and non-HW (black). The hatched area in (a) denotes the magnitude of the synergies between urban heat islands and heat waves. The dotted areas in (b) and (c) denote one standard deviations of urban and rural 2-m temperatures under HW (light red) and non-HW (light gray), respectively. The shaded areas denote 0550–0650 LST (light blue) and 1810–1930 LST (light red).

temperature especially at levels above ~ 2 km, RMSE being $0.92 ^{\circ}\text{C}$, but exhibits a good performance in simulating the temporal variation of air temperature profile with R of 0.997 (Fig. 5a and b). The wind speed tends to be underestimated particularly at levels above ~ 2 km, RMSE being 1.73 m s^{-1} , but the temporal variation of wind speed profile is satisfactorily reproduced with R of 0.90 (Fig. 5c and d). The temporal variation of wind direction profile is also satisfactorily simulated with R of 0.73 (Fig. 5e and f), fairly capturing changes in wind patterns during the HW event. Overall, the validation results suggest that the WRF model well simulates thermal and wind environments throughout the simulation period. Therefore, the simulation data are suitable for examining the UHI–HW synergies occurring in Seoul during the HW event.

3.3. Diurnal evolution of UHI–HW synergies

In this subsection, the diurnal evolution of the UHI–HW synergies is examined. Note that during the analysis period, the times of sunrise and sunset are ~ 0520 LST and ~ 2000 LST, respectively. Fig. 6a shows the diurnal variations of UHI intensities under HW and non-HW as well as the diurnal variation of ΔT_{syn} . Compared to observations, the simulated UHI intensity is generally stronger under both HW and non-HW (Supplementary Material Fig. S2a) while the simulated UHI–HW synergies are weaker (Supplementary Material Fig. S2b). Nevertheless, the diurnal evolution of the simulated UHI–HW synergies is in accordance with that of the observed UHI–HW synergies characterized by rapid

weakening in early morning and rapid strengthening in early evening (Supplementary Material Fig. S2b). Consistent with findings from numerous cities (Du et al., 2021; Meili et al., 2022), the nighttime UHI intensities are higher than the daytime UHI intensities (Fig. 6a), with mean differences between the nighttime and daytime being 2.86 and $1.91 ^{\circ}\text{C}$ under HW and non-HW, respectively. The daily maximum UHI intensity reaches $5.07 ^{\circ}\text{C}$ under HW and $4.02 ^{\circ}\text{C}$ under non-HW, and the daily minimum UHI intensity is $1.47 ^{\circ}\text{C}$ under HW and $1.25 ^{\circ}\text{C}$ under non-HW. It is evident that ΔT_{syn} is positive except during 1740–1840 LST, meaning that the UHI–HW synergies persist for almost the entire day (Fig. 6a). ΔT_{syn} exhibits a significant diurnal variation in which ΔT_{syn} rapidly strengthens during 1810–1930 LST and rapidly diminishes during 0550–0650 LST, similar to the diurnal pattern of the UHI–HW synergies typically found in Seoul (Park et al., 2023) as well as those in other large cities (Ramamurthy et al., 2017; Jiang et al., 2019; Ma et al., 2024; Syed Mahbar and Kusaka, 2024). As a result, ΔT_{syn} is prominent during the nighttime ($1.10 ^{\circ}\text{C}$) but is weak during the daytime ($0.15 ^{\circ}\text{C}$).

The diurnal variations of urban and rural 2-m temperatures are presented in Fig. 6b and c, respectively. The diurnal variations of both urban and rural 2-m temperatures are clear under HW and non-HW, with the rural 2-m temperature showing larger variations than the urban 2-m temperature (Fig. 6b and c). During 1810–1930 LST when ΔT_{syn} rapidly increases, the rural 2-m temperature declines much more steeply under HW than under non-HW while the urban 2-m temperature declines at similar rates under HW and non-HW. Meanwhile, during 0550–0650 LST when ΔT_{syn} rapidly decreases, the rural 2-m

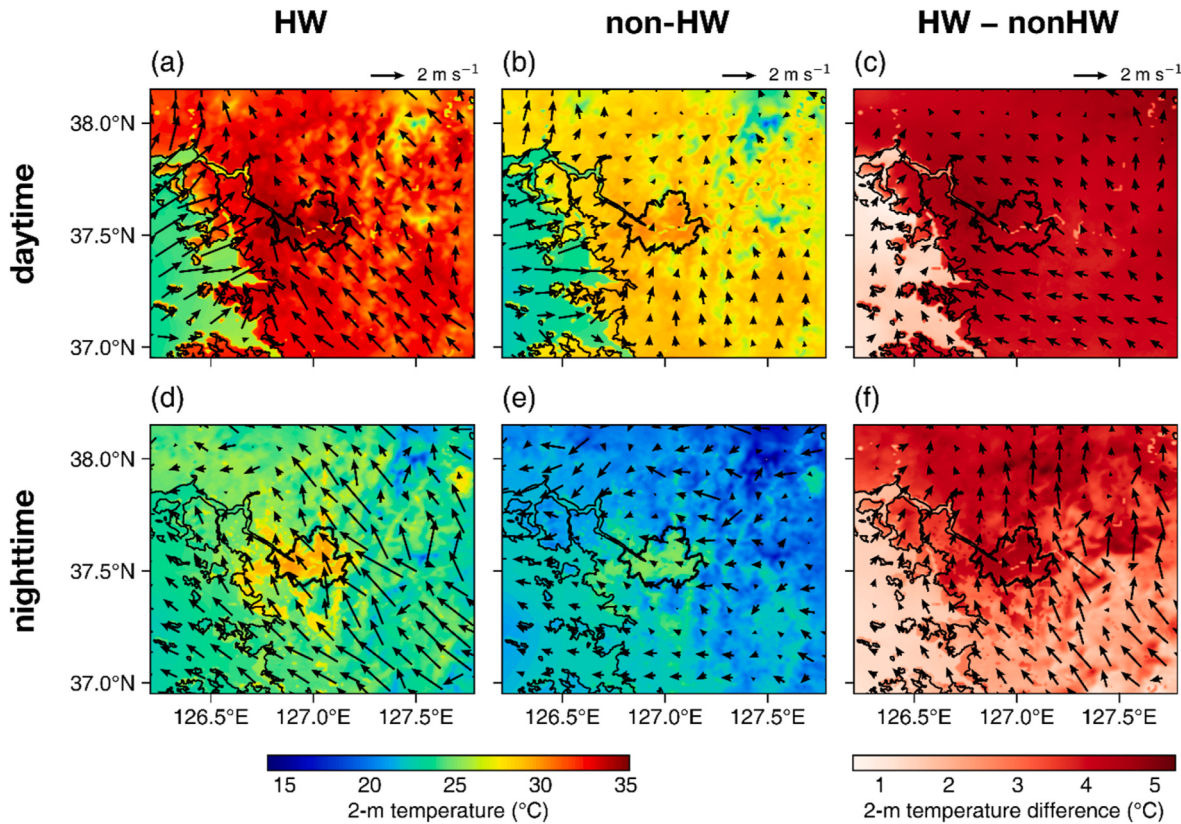


Fig. 7. Fields of daytime (1200–1700 LST) mean 2-m temperature and 10-m horizontal wind vector under (a) HW and (b) non-HW and (c) their respective differences (HW minus non-HW). Fields of nighttime (0000–0500 LST) mean 2-m temperature and 10-m horizontal wind vector under (d) HW and (e) non-HW and (f) their respective differences (HW minus non-HW). The administrative boundary of Seoul is indicated by the thick black solid line.

temperature increases even more sharply under HW than under non-HW while the urban 2-m temperature increases at similar rates under HW and non-HW. Thus, the different HW-induced changes in temperature evolution during these periods between the urban and rural areas lead to significant variations in ΔT_{syn} .

Fig. 7 presents the daytime and nighttime mean fields of 2-m temperature and 10-m wind vector under HW and non-HW and their respective differences. Under HW, southeasterly winds dominate during both daytime and nighttime, influenced by the high-pressure system over the Korean Peninsula (Fig. 7a and d). Seoul, the main urban area, is noticeably warmer than its surrounding rural areas due to background UHIs and UHI-HW synergies. Over the Yellow Sea located to the west of Seoul, the sea breeze well develops during the daytime (Fig. 7a). Under non-HW, winds are generally weak during both daytime and nighttime (Fig. 7b and e). The sea breeze appears during the daytime (Fig. 7b), and the land breeze prevails during the nighttime (Fig. 7e). Because of the presence of background UHIs, Seoul exhibits higher 2-m temperature than its surrounding rural areas.

Compared to non-HW, the 2-m temperatures are significantly elevated under HW throughout the analysis area (Fig. 7c and f). During the daytime, the HW-induced warming is somewhat similar in the urban and rural areas (Fig. 7c), which is indicative of relatively weak ΔT_{syn} . On the other hand, the HW-induced warming during the nighttime is pronounced in Seoul (Fig. 7f), which is a sign of relatively strong ΔT_{syn} . In addition, the HW-induced warming is more pronounced north of Seoul than south of Seoul during the nighttime. This suggests that the UHI-HW synergies influence downwind areas along the prevailing winds.

3.4. Changes in urban and rural PBL structures and surface energy balances

In this subsection, the responses of PBLs and surface energy balances in the urban and rural areas to HWs are investigated. Fig. 8 shows the HW-induced changes in urban and rural potential temperature profiles and PBL heights during the daytime and nighttime. During the daytime, both urban and rural convective boundary layers (CBLs) well develop regardless of HW and non-HW (Fig. 8a and b). Compared to non-HW, the daytime mean PBL height under HW is higher by 280 m in the urban area and by 196 m in the rural area. The HW-induced warming is nearly uniform across the CBL in both urban and rural areas, and the urban CBL experiences a greater warming (4.51 K) under HW than the rural CBL (4.42 K). The HW-induced warming of the rural CBL is comparable to that found in observations (Supplementary Material Fig. S3a). During the nighttime, both urban and rural stable boundary layers (SBLs) develop irrespective of HW and non-HW (Fig. 8c and d). The urban SBL is much less stable than the rural SBL, likely due to UHIs. The nighttime mean PBL height is lower under HW than under non-HW by 35 m in the urban area and by 11 m in the rural area. The HW-induced warming is greater in the residual layer (RL) than in the SBL in both urban and rural areas, making the SBL more stable and the RL more energized under HW. This characteristic is also found in observations (Supplementary Material Fig. S3b). The peak differences in urban and rural potential temperatures between HW and non-HW are 5.10 and 5.07 K, respectively. The changes in daytime and nighttime PBL structures during the HW event (Fig. 8) are in accordance with those found in previous studies (Miralles et al., 2014; Zhang et al., 2020).

Fig. 9 presents the diurnal variations of vertical velocity profile under HW and non-HW. In the urban area, strong upward motions appear during the daytime under both HW and non-HW (Fig. 9a and b).

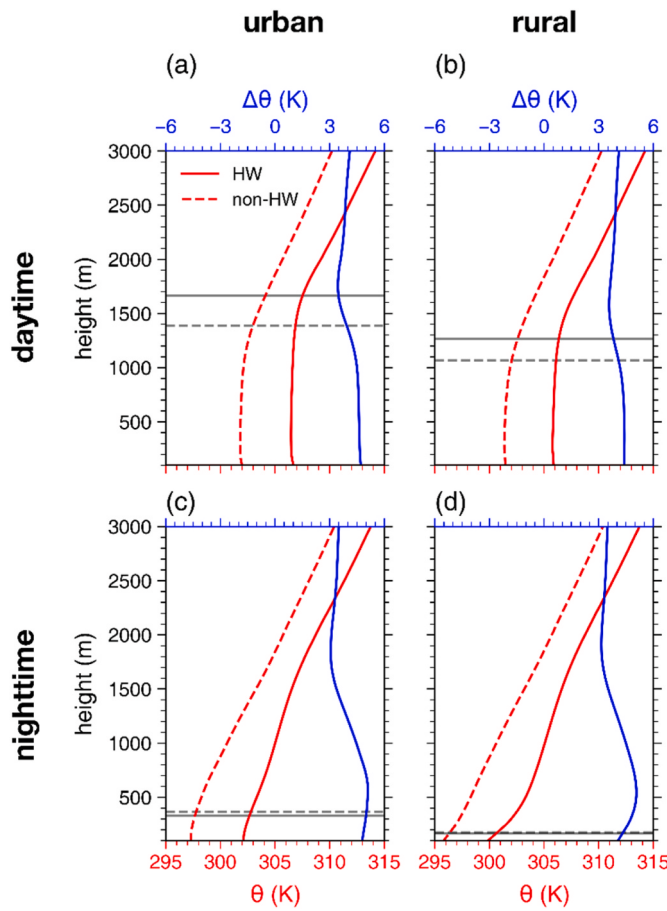


Fig. 8. Vertical profiles of daytime (1200–1700 LST) mean (a) urban and (b) rural potential temperatures (red) under HW (solid) and non-HW (dashed) and their respective differences (blue) (HW minus non-HW). Vertical profiles of nighttime (0000–0500 LST) mean (c) urban and (d) rural potential temperatures (red) under HW (solid) and non-HW (dashed) and their respective differences (blue) (HW minus non-HW). The gray horizontal lines denote the mean PBL heights under HW (solid) and non-HW (dashed).

Even during the nighttime, weak upward motions appear. The persistent upward vertical velocities throughout the day are attributed to UHIs which make the urban PBL less stable than the rural PBL (Barlow et al., 2015; Varentsov et al., 2023). Compared to non-HW, the upward motions under HW are generally stronger within the PBL (Fig. 9c). The maximum urban vertical velocity difference between HW and non-HW is found at 1620 LST, being 0.04 m s^{-1} . It was revealed that the urban PBL is more energized and well develops during HWs (Ramamurthy et al., 2017; Wu et al., 2019; Xin et al., 2024). In contrast to the urban area, the upward motions in the rural area during the daytime are weak under both HW and non-HW (Fig. 9d and e). Furthermore, subsiding motions appear in the rural SBL during the nighttime. The subsiding motions in the rural SBL are evident in the rural areas with elevated terrains (Fig. 1c and Supplementary Material Fig. S4a–c). These subsiding motions are attributed to compensating subsidence resulting from the diverging katabatic flows which develop in the rural areas with elevated terrains as the rural areas cool (Supplementary Material Fig. S4a–c). R between mean horizontal wind divergence at the lowest model level and terrain height (mean 2-m temperature) during the nighttime in the rural area is 0.54 (-0.59) under HW and 0.55 (-0.49) under non-HW and is statistically significant at $p < 0.001$, the diverging katabatic flows being prominent over the rural areas with elevated terrains and relatively low temperature. The diverging katabatic flows can result in horizontal cold advection in the rural areas with low-lying terrains, and the subsidence advecting warm air from the RL into the SBL leads to vertical warm advection in the rural areas with elevated terrains. The nighttime mean vertical velocity within the rural SBL is -0.10 m s^{-1} under HW and -0.07 m s^{-1} under non-HW. Compared to non-HW, both daytime ascent and nighttime subsidence are intensified under HW (Fig. 9f). It is also noticeable that the rural RL is more energized under HW, consistent with Fig. 8d. The formation of excessively warm and deep RL during HWs is well documented (Miralles et al., 2014; Wang and Li, 2019).

Next, the HW-induced changes in urban and rural surface energy balances are investigated:

$$\Delta Q^* = \Delta Q_H + \Delta Q_E + \Delta Q_C \quad (5)$$

where ΔQ^* , ΔQ_H , ΔQ_E , and ΔQ_C are the differences in net radiation, sensible heat flux, latent heat flux, and storage heat flux between HW and non-HW (HW minus non-HW), respectively. Fig. 10 shows the diurnal variations of urban and rural ΔQ^* , ΔQ_H , ΔQ_E , and ΔQ_C . The

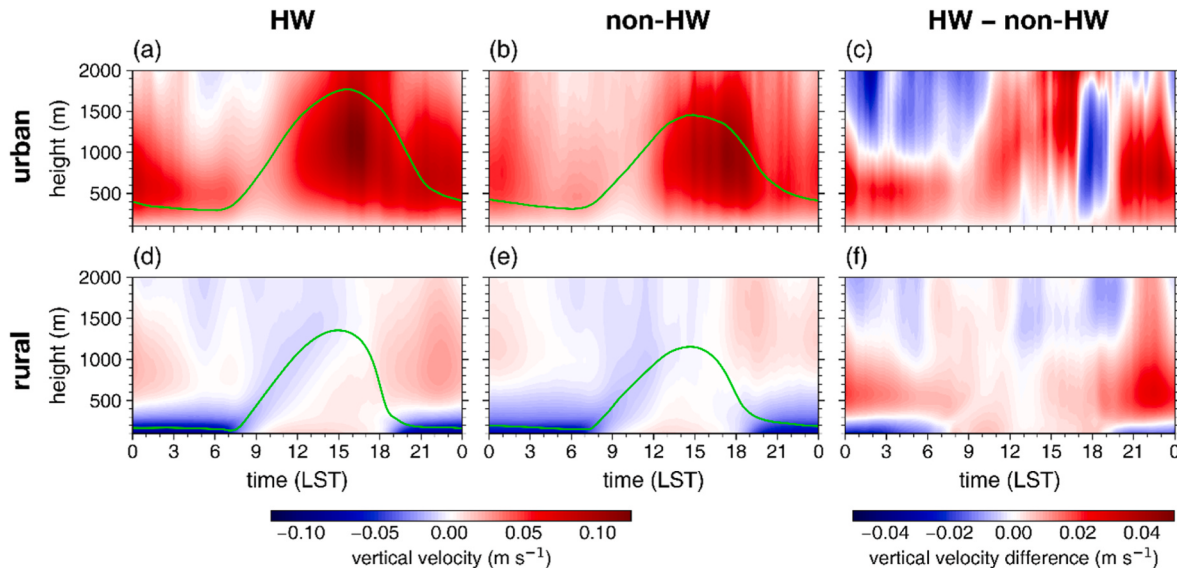


Fig. 9. Time-height cross sections of vertical velocities under (a) HW and (b) non-HW and (c) their differences (HW minus non-HW) in the urban area. Time-height cross sections of vertical velocities under (d) HW and (e) non-HW and (f) their differences (HW minus non-HW) in the rural area. The green solid line denotes the PBL height.

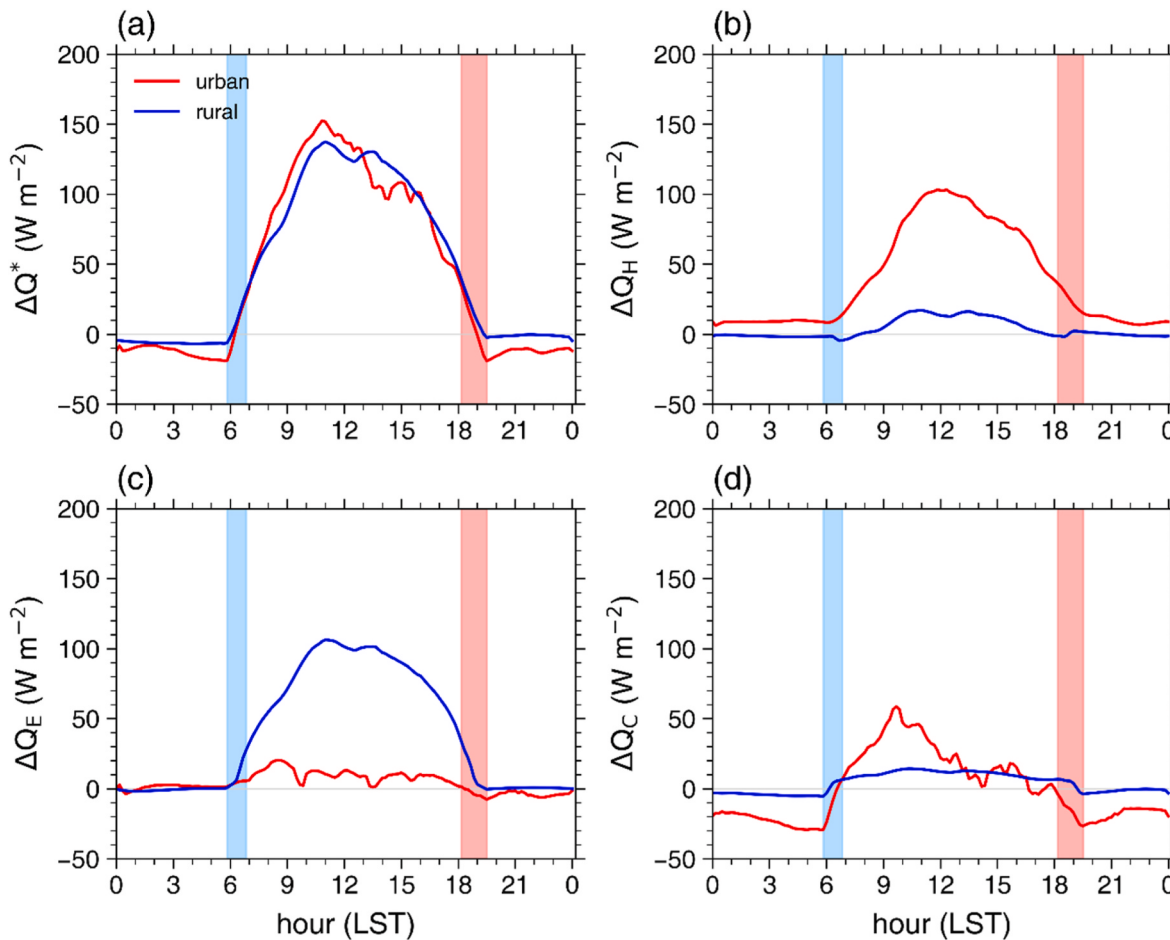


Fig. 10. Diurnal variations of the differences in net radiation (ΔQ^*), sensible heat flux (ΔQ_H), latent heat flux (ΔQ_E), and storage heat flux (ΔQ_C) between HW and non-HW (HW minus non-HW) in the urban (red) and rural (blue) areas. The shaded areas denote 0550–0650 LST (light blue) and 1810–1930 LST (light red).

positive ΔQ^* is prominent in the morning and daytime in both urban and rural areas (Fig. 10a), resulting from greater incoming shortwave radiation under clearer weather conditions during HW (Kong et al., 2023; Syed Mahbar and Kusaka, 2024). During the nighttime, both urban and rural ΔQ^* are negative, which is attributed to greater emitted longwave radiation under HW compared to non-HW. The positive ΔQ^* is primarily partitioned into ΔQ_H in the urban area but into ΔQ_E in the rural area (Fig. 10b and c). These contrasting changes in turbulent heat fluxes under HW between the urban and rural areas are also found in previous studies (Li et al., 2015; He et al., 2020). Both urban and rural ΔQ_C are positive in the morning and daytime and are negative in the evening and nighttime (Fig. 10d). This shows that more heat is stored into the subsurface and is subsequently released under HW than under non-HW. The urban ΔQ_C generally exhibits larger magnitudes than the rural ΔQ_C , meaning that excessive heat storage under HW is more prominent in the urban area than in the rural area. The remarkable increase in urban heat storage during HWs is a well-known characteristic response of urban surfaces to HWs compared to rural surfaces (Li and Bou-Zeid, 2013; Sun et al., 2017; Li et al., 2024).

During both 1810–1930 LST and 0550–0650 LST when ΔT_{syn} undergoes significant variations, the magnitude of urban ΔQ_H (ΔQ_E) is larger (smaller) than that of rural ΔQ_H (ΔQ_E) (Fig. 10b and c), the urban-rural contrasts in both sensible and latent heat fluxes being larger due to HW. The urban ΔQ_C steeply decreases and is negative during 1810–1930 LST and steeply increases and becomes positive during 0550–0650 LST (Fig. 10d), revealing the prominent increase in the release of stored heat in early evening and the prominent increase in the rate of increase in storage heat flux in early morning, respectively. Meanwhile, the rural

ΔQ_C exhibits very small magnitudes during both periods. These differing changes in urban and rural surface energy balances can differently contribute to the near-surface thermodynamic energy budgets under HW. In the next subsection, HW-induced changes in urban and rural near-surface thermodynamic energy budgets (Eq. (4)) are investigated to elucidate the temporal evolution of ΔT_{syn} during these periods.

3.5. Changes in urban and rural near-surface thermodynamic energy budgets

Fig. 11a shows the urban and rural $\Delta(\partial T/\partial t)$, $\Delta(-u\partial T/\partial x - v\partial T/\partial y)$, $\Delta(-w\partial T/\partial z)$, $\Delta(\omega a/c_p)$, and $\Delta(Q/c_p)$ averaged over 1810–1930 LST. The mean urban and rural $\Delta(\partial T/\partial t)$ during 1810–1930 LST are 0.13 and -0.68 K h^{-1} , respectively. This reveals that the rural cooling is considerably enhanced under HW while the urban cooling alters slightly, resulting in the increase in ΔT_{syn} during 1810–1930 LST. The mean urban $\Delta(-u\partial T/\partial x - v\partial T/\partial y)$ during 1810–1930 LST is 0.07 K h^{-1} , which is opposite to the mean rural $\Delta(-u\partial T/\partial x - v\partial T/\partial y)$ of -0.12 K h^{-1} . During 1810–1930 LST, southerly/southwesterly winds predominantly appear over Seoul under HW (Supplementary Material Fig. S5a–c). As a result, Seoul is influenced by advection from urban areas located south/southwest (Fig. 1d) and thus the urban advective cooling is reduced. Conversely, the rural advective cooling is enhanced under HW, attributable to higher regional wind speeds compared to non-HW. These regional wind characteristics during these hours under HW lead to different HW-induced changes in temperature tendency due to horizontal advection between the urban and rural areas, contributing to the urban-rural contrast in $\Delta(\partial T/\partial t)$. The mean $\Delta(-w\partial T/\partial z)$ and $\Delta(\omega a/c_p)$

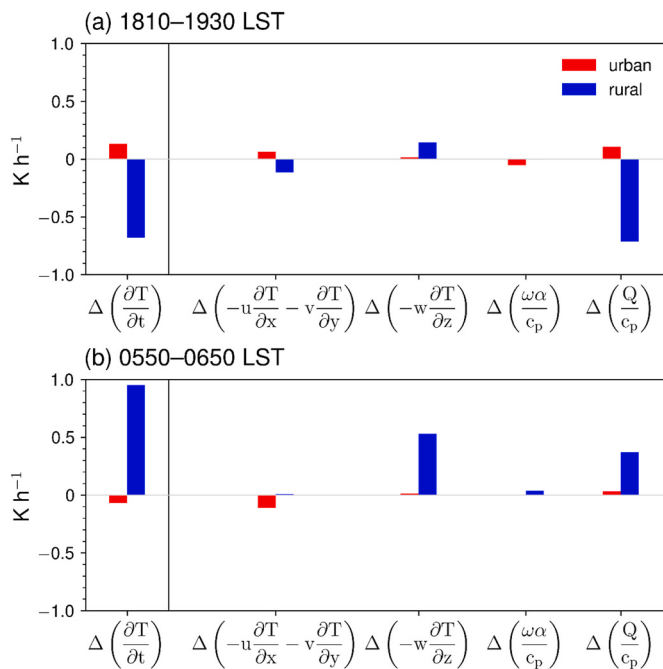


Fig. 11. Mean differences in local temperature tendency ($\Delta(\partial T/\partial t)$) and temperature tendencies due to horizontal advection ($\Delta(-u\partial T/\partial x - v\partial T/\partial y)$), vertical advection ($\Delta(-w\partial T/\partial z)$), adiabatic processes ($\Delta(\omega\alpha/c_p)$), and diabatic processes ($\Delta(Q/c_p)$) between HW and non-HW (HW minus non-HW) in the urban (red) and rural (blue) areas during (a) 1810–1930 LST and (b) 0550–0650 LST.

during 1810–1930 LST exhibit relatively small urban-rural differences of -0.13 and $-0.06 K h^{-1}$, respectively. The most pronounced urban-rural contrast during 1810–1930 LST is found for $\Delta(Q/c_p)$, its mean value being $0.10 K h^{-1}$ in the urban area and $-0.71 K h^{-1}$ in the rural area. The large negative rural $\Delta(Q/c_p)$ can result from the enhancement of rural radiative cooling under clearer weather conditions during HW. In the urban area, the small positive $\Delta(Q/c_p)$ might be attributed to the pronounced increases in both release of stored heat through the sensible heat flux and turbulent mixing (Fig. 10b and d and Supplementary

Material Fig. S6). Hence, the increase in ΔT_{syn} during 1810–1930 LST primarily results from the different changes in urban and rural diabatic heating/cooling processes (Q/c_p) in response to HW (Fig. 11a). The difference in changes in urban and rural $-u\partial T/\partial x - v\partial T/\partial y$ under HW is secondly important for the increase in ΔT_{syn} .

Fig. 11b is the same as Fig. 11a except over 0550–0650 LST. The mean urban and rural $\Delta(\partial T/\partial t)$ during 0550–0650 LST are -0.07 and $0.95 K h^{-1}$, respectively. This reveals that the rural warming is considerably enhanced under HW whereas the urban warming exhibits marginal changes, leading to the decrease in ΔT_{syn} during 0550–0650 LST. The mean urban $\Delta(-u\partial T/\partial x - v\partial T/\partial y)$ is $-0.11 K h^{-1}$ during 0550–0650 LST, the mean rural $\Delta(-u\partial T/\partial x - v\partial T/\partial y)$ being only $0.01 K h^{-1}$. The urban advective cooling is enhanced during 0550–0650 LST under HW as the urban-rural contrast in 2-m temperature and wind speed become larger than under non-HW (Supplementary Material Fig. S5d-f). In the rural area, the diverging katabatic flows are enhanced under HW as the nocturnal rural cooling strengthens (Supplementary Material Fig. S4d-f), whereas the horizontal warm advection from the urban areas is also enhanced (Supplementary Material Fig. S5d-f). This appears to lead the rural advective cooling to be only slightly altered under HW. The most pronounced urban-rural contrast is found for $\Delta(-w\partial T/\partial z)$, with its mean values of $0.01 K h^{-1}$ in the urban area and $0.53 K h^{-1}$ in the rural area. The large positive rural $\Delta(-w\partial T/\partial z)$ is due to the increase in the advection of warm air from the RL as the rural RL becomes excessively warmer (Fig. 8d) and the compensating subsidence resulting from the diverging katabatic flows becomes stronger (Fig. 9f and Supplementary Material Fig. S4d-f) under HW. The clearer weather conditions during HW contribute to the warmer RL and stronger subsidence by facilitating greater heat accumulation within the PBL during the daytime and by enhancing the nocturnal rural cooling, respectively. On the other hand, in the urban area, subsidence rarely occurs near the surface (Fig. 9a-c) owing to the relatively flat terrains (Fig. 1c) and persistent UHIs (Fig. 6a) and consequently the advection of warm air from the RL is marginal. The urban and rural $\Delta(\omega\alpha/c_p)$ during 0550–0650 LST exhibit small differences with the mean urban-rural difference of $-0.04 K h^{-1}$. During 0550–0650 LST, the rural diabatic heating is more intensified under HW than the urban diabatic heating, the mean urban and rural $\Delta(Q/c_p)$ during 0550–0650 LST being 0.03 and $0.37 K h^{-1}$, respectively. This can be due to that the greater

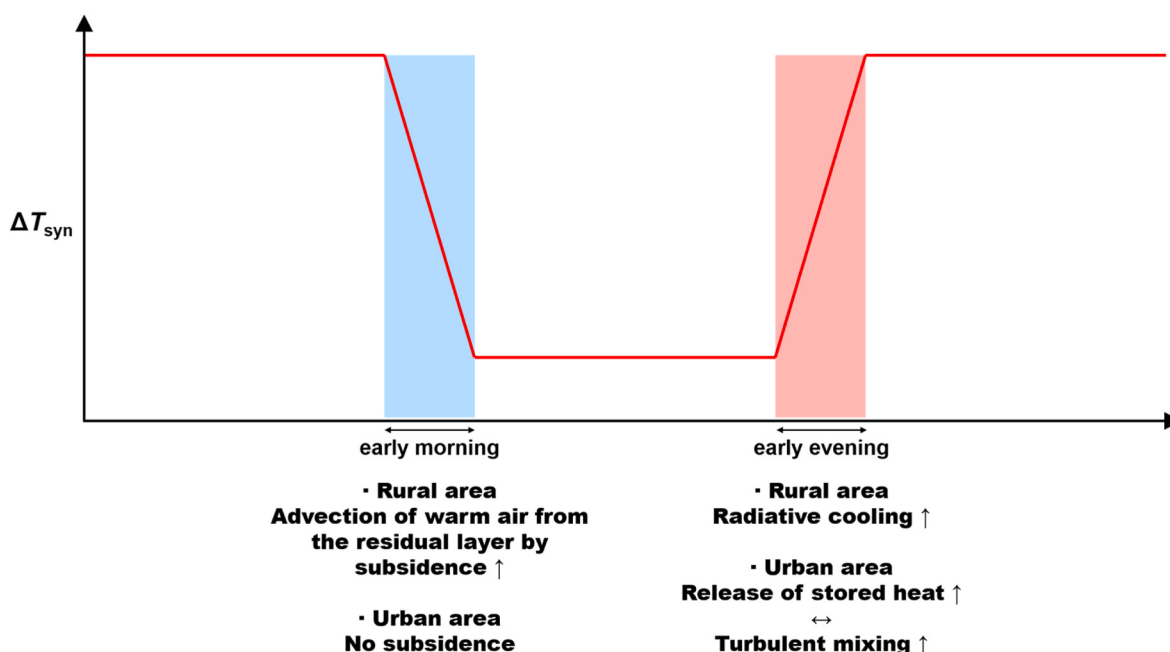


Fig. 12. Schematic diagram of the diurnal evolution of the synergies between urban heat islands and heat waves and its key physical processes found in this study.

absorbed radiation under HW more effectively intensifies the diabatic heating in the rural area than in the urban area where the rate of increase in storage heat flux substantially increases (Fig. 10d), contributing to the urban-rural contrast in $\Delta(\partial T/\partial t)$. Thus, the contrasting changes in urban and rural vertical motions and resultant advects ($-w\partial T/\partial z$) in response to HW are mainly responsible for the decrease in ΔT_{syn} during 0550–0650 LST, the different changes in urban and rural Q/c_p under HW being the secondly important cause.

4. Summary and conclusions

In this study, the diurnal evolution of the synergies between UHIs and HWs and its associated physical processes are examined using the WRF model. A 45-day simulation which includes an extreme HW event with strong UHI–HW synergies is conducted, and changes in urban and rural near-surface thermodynamic energy budgets under HW are investigated. The diurnal evolution of the UHI–HW synergies is characterized by rapid strengthening in early evening and rapid weakening in early morning, as found in many other large cities. In early evening, the rural diabatic cooling is clearly enhanced during HW under clearer weather conditions. In the urban area, both release of stored heat and turbulent mixing prominently increase under HW and thus the urban diabatic heating only slightly alters. These contrasting responses of urban and rural diabatic processes to HW are primarily responsible for the strengthening of the UHI–HW synergies in early evening. Meanwhile, in early morning, the advection of warm air from the rural RL by subsidence significantly increases under HW while the subsidence hardly appears within the urban PBL. These different responses of urban and rural PBL processes to HW are mainly associated with the weakening of the UHI–HW synergies in early morning. For the diurnal evolution of the UHI–HW synergies, the persistently clearer weather conditions during HW act as a background state in which the urban and rural near-surface thermodynamic processes alter differently. Fig. 12 summarizes the key processes associated with the diurnal evolution of the UHI–HW synergies.

This study unravels underlying physical processes for the diurnal evolution of the UHI–HW synergies through the analysis of urban and rural near-surface thermodynamic energy budget changes during HWs, not attempted in previous studies. To quantify the thermodynamic energy budget terms (Eq. (3)), the 2-m temperature, which is diagnosed in the WRF model, is used and thus the diabatic heating/cooling by physical processes which include radiative processes, turbulent mixing, and sensible heating is quantified through the residual approach. For a more advanced analysis of urban and rural thermodynamic energy budget changes under HW, an application of a novel method to physically quantify near-surface thermodynamic energy budget changes due to various physical processes is needed.

In this study, a high-resolution anthropogenic heat dataset estimated for Seoul and its surrounding areas is employed to better simulate the effects of anthropogenic heat on UHIs. However, the anthropogenic heat dataset used for the simulation does not take into account changes in the emission of anthropogenic heat due to HWs. Several previous studies demonstrated that the emission of anthropogenic heat noticeably increases during HWs mainly due to increased energy consumptions (Luo et al., 2020; Chen et al., 2023) and that the increase in anthropogenic heat during HWs significantly affects the UHI–HW synergies (Zhao et al., 2018; Khan et al., 2025). To well simulate and disentangle the effects of changes in anthropogenic heat flux during HWs and their importance on the UHI–HW synergies, the use of a building energy model (e.g., Salamanca et al., 2010) which can simulate changes in anthropogenic heat in response to HWs is required.

This study relies on a single HW event in Seoul with strong UHI–HW synergies. Given that the characteristics of the UHI–HW synergies may vary depending on meteorological and soil conditions during HWs (Park et al., 2023; Kim et al., 2024a; Zhao et al., 2024), investigating various HW events would deepen the understanding of the characteristics of the

UHI–HW synergies and key meteorological and soil-related factors influencing them. In addition, in this study, a pre-HW period and a post-HW period with overall similar weather conditions to the climatological mean are considered to identify the effects of the presence of HWs. For a more robust identification of the HW-induced effects, simulating various cases to characterize normal summer conditions is required.

Finally, it should be noted that the diurnal pattern of the UHI–HW synergies can vary depending on geographic features of cities. For instance, in several coastal cities, it was found that the daytime UHI–HW synergies are more pronounced than the nighttime UHI–HW synergies (e.g., Founda and Santamouris, 2017; Ao et al., 2019). An extensive investigation of the diurnal evolution of the UHI–HW synergies and its key drivers in cities with various geographic settings can make it possible to better understand the influence of geographic features on the UHI–HW synergies.

CRediT authorship contribution statement

Kyeongjoo Park: Writing – review & editing, Writing – original draft, Visualization, Validation, Methodology, Investigation, Formal analysis, Data curation. **Jong-Jin Baik:** Writing – review & editing, Supervision, Methodology, Formal analysis, Conceptualization.

Declaration of competing interest

The authors declare that they have no known competing financial interests or personal relationships that could have appeared to influence the work reported in this paper.

Acknowledgements

We would like to express our gratitude to two anonymous reviewers for providing valuable comments that help to improve this work. This work was supported by the National Research Foundation of Korea (NRF) under grant RS-2025-00562044.

Appendix A. Supplementary data

Supplementary data to this article can be found online at <https://doi.org/10.1016/j.wace.2026.100854>.

Data availability

Data will be made available on request.

References

- An, N., Dou, J., González-Cruz, J.E., Bornstein, R.D., Miao, S., Li, L., 2020. An observational case study of synergies between an intense heat wave and the urban heat island in Beijing. *J. Appl. Meteorol. Climatol.* 59, 605–620.
- Ao, X., Wang, L., Zhi, X., Gu, W., Yang, H., Li, D., 2019. Observed synergies between urban heat islands and heat waves and their controlling factors in Shanghai, China. *J. Appl. Meteorol. Climatol.* 58, 1955–1972.
- Baik, J.-J., Lim, H., Han, B.-S., Jin, H.-G., 2022. Cool-roof effects on thermal and wind environments during heat waves: a case modeling study in Seoul, South Korea. *Urban Clim.* 41, 101044.
- Barlow, J.F., Halios, C.H., Lane, S.E., Wood, C.R., 2015. Observations of urban boundary layer structure during a strong urban heat island event. *Environ. Fluid Mech.* 15, 373–398.
- Barriopedro, D., García-Herrera, R., Ordóñez, C., Miralles, D.G., Salcedo-Sanz, S., 2023. Heat waves: physical understanding and scientific challenges. *Rev. Geophys.* 61, e2022RG000780.
- Basara, J.B., Basara, H.G., Illston, B.G., Crawford, K.C., 2010. The impact of the urban heat island during an intense heat wave in Oklahoma City. *Adv. Meteorol.* 2010, 230365.
- Beck, H.E., Zimmermann, N.E., McVicar, T.R., Vergopolan, N., Berg, A., Wood, E.F., 2018. Present and future Köppen-Geiger climate classification maps at 1-km resolution. *Sci. Data* 5, 180214.
- Chan, S.C., Nigam, S., 2009. Residual diagnosis of diabatic heating from ERA-40 and NCEP reanalyses: intercomparisons with TRMM. *J. Clim.* 22, 414–428.

- Chen, B., Wu, C., Song, X., Zheng, Y., Lu, M., Yang, H., Wu, X., Zhao, X., Lu, Z., Luo, T., Liu, X., 2023. Anthropogenic heat release due to energy consumption exacerbates European summer extreme high temperature. *Clim. Dyn.* 61, 3831–3843.
- Chen, F., Dudhia, J., 2001. Coupling an advanced land surface-hydrology model with the Penn State-NCAR MM5 modeling system. Part I: model implementation and sensitivity. *Mon. Weather Rev.* 129, 569–585.
- Chen, F., Kusaka, H., Bornstein, R., Ching, J., Grimmond, C.S.B., Grossman-Clarke, S., Loridan, T., Manning, K.W., Martilli, A., Miao, S., Sailor, D., Salamanca, F.P., Taha, H., Tewari, M., Wang, X., Wyszogrodzki, A.A., Zhang, C., 2011. The integrated WRF/urban modelling system: development, evaluation, and applications to urban environmental problems. *Int. J. Climatol.* 31, 273–288.
- Cuce, P.M., Cuce, E., Santamouris, M., 2025. Towards sustainable and climate-resilient cities: mitigating urban heat islands through green infrastructure. *Sustainability* 17, 1303.
- Cui, F., Hamdi, R., Kuang, W., Yang, T., He, H., Termonia, P., De Maeyer, P., 2023. Interactions between the summer urban heat islands and heat waves in Beijing during 2000–2018. *Atmos. Res.* 291, 106813.
- Deilami, K., Kamruzzaman, M., Liu, Y., 2018. Urban heat island effect: a systematic review of spatio-temporal factors, data, methods, and mitigation measures. *Int. J. Appl. Earth Obs. Geoinf.* 67, 30–42.
- Du, H., Zhan, W., Liu, Z., Li, J., Li, L., Lai, J., Miao, S., Huang, F., Wang, C., Wang, C., Fu, H., Jiang, L., Hong, F., Jiang, S., 2021. Simultaneous investigation of surface and canopy urban heat islands over global cities. *ISPRS J. Photogramm. Remote Sens.* 181, 67–83.
- Dudhia, J., 1989. Numerical study of convection observed during the Winter Monsoon Experiment using a mesoscale two-dimensional model. *J. Atmos. Sci.* 46, 3077–3107.
- Farr, T.G., Rosen, P.A., Caro, E., Crippen, R., Duren, R., Hensley, S., Kobrick, M., Paller, M., Rodriguez, E., Roth, L., Seal, D., Shaffer, S., Shimada, J., Umland, J., Werner, M., Oskin, M., Burbank, D., Alsdorf, D., 2007. The Shuttle Radar Topography Mission. *Rev. Geophys.* 45, 2005RG000183.
- Founda, D., Santamouris, M., 2017. Synergies between Urban Heat Island and Heat Waves in Athens (Greece), during an extremely hot summer (2012). *Sci. Rep.* 7, 10973.
- Fu, Q., Zheng, Z., Sarker, M.N.I., Lv, Y., 2024. Combating urban heat: systematic review of urban resilience and adaptation strategies. *Heliyon* 10, e37001.
- Gao, X., Yin, J., Yun, Y., Zhang, S., 2025. On the mechanism of the Hainan Island modulating extreme rainfall along the South China coast via thermodynamic forcing. *Clim. Dyn.* 63, 163.
- Guindon, S.-M., Nirupama, N., 2015. Reducting risk from urban heat island effects in cities. *Nat. Hazards* 77, 823–831.
- He, X., Wang, J., Feng, J., Yan, Z., Miao, S., Zhang, Y., Xia, J., 2020. Observational and modeling study of interactions between urban heat island and heatwave in Beijing. *J. Clean. Prod.* 247, 119169.
- Hersbach, H., Bell, B., Berrisford, P., Hirahara, S., Horányi, A., Muñoz-Sabater, J., Nicolas, J., Peubey, C., Radu, R., Schepers, D., Simmons, A., Soci, C., Abdalla, S., Abellán, X., Balsamo, G., Bechtold, P., Blavatik, G., Bidlot, J., Bonavita, M., De Chiara, G., Dahlgren, P., Dee, D., Diamantakis, M., Dragani, R., Flemming, J., Forbes, R., Fuentes, M., Geer, A., Haimberger, L., Healy, S., Hogan, R.J., Hólm, E., Janisková, M., Keeley, S., Laloyaux, P., Lopez, P., Lupu, C., Radnoti, G., de Rosnay, P., Rozum, I., Vamborg, F., Villaume, S., Thépaut, J.-N., 2020. The ERA5 global reanalysis. *Q. J. R. Meteorol. Soc.* 146, 1999–2049.
- Hong, S.-Y., Lim, J.-O.J., 2006. The WRF single-moment 6-class microphysics scheme (WSM6). *J. Korean Meteorol. Soc.* 42, 129–151.
- Hong, S.-Y., Noh, Y., Dudhia, J., 2006. A new vertical diffusion package with an explicit treatment of entrainment processes. *Mon. Weather Rev.* 134, 2318–2341.
- Hu, S., Zhou, T., Wu, B., Chen, X., 2023. Seasonal prediction of the record-breaking northward shift of the western Pacific subtropical high in July 2021. *Adv. Atmos. Sci.* 40, 410–427.
- Huang, K., Li, X., Liu, X., Seto, K.C., 2019. Projecting global urban land expansion and heat island intensification through 2050. *Environ. Res. Lett.* 14, 114037.
- Jiang, S., Lee, X., Wang, J., Wang, K., 2019. Amplified urban heat islands during heat wave periods. *J. Geophys. Res. Atmos.* 124, 7797–7812.
- Jiménez, P.A., Dudhia, J., González-Rouco, J.F., Navarro, J., Montávez, J.P., García-Bustamante, E., 2012. A revised scheme for the WRF surface layer formulation. *Mon. Weather Rev.* 140, 898–918.
- Kain, J.S., 2004. The Kain-Fritsch convective parameterization: an update. *J. Appl. Meteorol.* 43, 170–181.
- Khan, A., Vasilakopoulou, K., Santamouris, M., 2025. Exploring the potential impacts of anthropogenic heating on urban climate during heatwaves. *Sci. Rep.* 15, 3908.
- Kim, D.-H., Park, K., Baik, J.-J., Jin, H.-G., Han, B.-S., 2024a. Contrasting interactions of urban heat islands with dry and moist heat waves and their implications for urban heat stress. *Urban Clim.* 56, 102050.
- Kim, D.W., Lee, S., Clark, J.P., Feldstein, S.B., 2024b. Benchmark thermodynamic contributors to the growth and decay of the regional extreme surface temperature. *J. Clim.* 37, 2347–2359.
- Kim, H., Choi, N., Lee, M.-I., Tak, S., Cha, D.-H., Min, S.-K., 2024c. Causes on the 2018 record-breaking heatwave in South Korea: compound impacts from recurrent large-scale atmospheric teleconnections. *Environ. Res. Lett.* 19, 124064.
- Kong, J., Zhao, Y., Carmeliet, J., Lei, C., 2021. Urban heat island and its interaction with heatwaves: a review of studies on mesoscale. *Sustainability* 13, 10923.
- Kong, J., Zhao, Y., Strelbel, D., Gao, K., Carmeliet, J., Lei, C., 2023. Understanding the impact of heatwave on urban heat in greater Sydney: temporal surface energy budget change with land types. *Sci. Total Environ.* 903, 166374.
- Kosaka, Y., Nakamura, H., 2006. Structure and dynamics of the summertime Pacific-Japan teleconnection pattern. *Q. J. R. Meteorol. Soc.* 132, 2009–2030.
- Kubota, H., Kosaka, Y., Xie, S.-P., 2016. A 117-year long index of the Pacific-Japan pattern with application to interdecadal variability. *Int. J. Climatol.* 36, 1575–1589.
- Lee, S.-H., Kim, S.-T., 2015. Estimation of anthropogenic heat emission over South Korea using a statistical regression method. *Asia-Pac. J. Atmos. Sci.* 51, 157–166.
- Li, D., Bou-Zeid, E., 2013. Synergistic interactions between urban heat islands and heat waves: the impact in cities is larger than the sum of its parts. *J. Appl. Meteorol. Climatol.* 52, 2051–2064.
- Li, D., Sun, T., Liu, M., Yang, L., Wang, L., Gao, Z., 2015. Contrasting responses of urban and rural surface energy budgets to heat waves explain synergies between urban heat islands and heat waves. *Environ. Res. Lett.* 10, 054009.
- Li, D., Wang, L., Liao, W., Sun, T., Katul, G., Bou-Zeid, E., Maronga, B., 2024. Persistent urban heat. *Sci. Adv.* 10, eadj7398.
- Lipson, M.J., Grimmond, S., Best, M., Abramowitz, G., Coutts, A., Tapper, N., Baik, J.-J., Beyers, M., Blunn, L., Boussetta, S., Bou-Zeid, E., De Kauwe, M.G., de Munck, C., Demuzere, M., Faticchi, S., Fortuniak, K., Han, B.-S., Hendry, M.A., Kikegawa, Y., Kondo, H., Lee, D.-I., Lee, S.-H., Lemonsu, A., Machado, T., Manoli, G., Martilli, A., Masson, V., McNorton, J., Meili, N., Meyer, D., Nice, K.A., Oleson, K.W., Park, S.-B., Roth, M., Schoetter, R., Simón-Moral, A., Steeneveld, G.-J., Sun, T., Takane, Y., Thatcher, M., Tsirigakis, A., Varentsov, M., Wang, C., Wang, Z.-H., Pitman, A.J., 2024. Evaluation of 30 urban land surface models in the Urban-PLUMBER project: phase 1 results. *Q. J. R. Meteorol. Soc.* 150, 126–169.
- Luo, F., Yang, Y., Zong, L., Bi, X., 2023. The interactions between urban heat island and heat waves amplify urban warming in Guangzhou, China: roles of urban ventilation and local climate zones. *Front. Environ. Sci.* 11, 1084473.
- Luo, X., Vahmani, P., Hong, T., Jones, A., 2020. City-scale building anthropogenic heating during heat waves. *Atmosphere* 11, 1206.
- Ma, X., Miao, S., Masson, V., Wurtz, J., Zhang, Y., Wang, J., Huang, X.-Y., Yan, C., 2024. The synergistic effects of urbanization and an extreme heatwave event on urban thermal environment in Paris. *Urban Clim.* 53, 101785.
- Marcotullio, P.J., Keßler, C., Fekete, B.M., 2022. Global urban exposure projections to extreme heatwaves. *Front. Built Environ.* 8, 947496.
- Martins, J.P.A., Cardoso, R.M., Soares, P.M.M., Trigo, I.F., Belo-Pereira, M., Moreira, N., Tomé, R., 2016. The summer diurnal cycle of coastal cloudiness over west Iberia using Meteosat/SEVIRI and a WRF regional climate model simulation. *Int. J. Climatol.* 36, 1755–1772.
- Matsumura, S., Sugimoto, S., Sato, T., 2015. Recent intensification of the western Pacific subtropical high associated with the East Asian summer monsoon. *J. Clim.* 28, 2873–2883.
- Meili, N., Paschalidis, A., Manoli, G., Faticchi, S., 2022. Diurnal and seasonal patterns of global urban dry islands. *Environ. Res. Lett.* 17, 054044.
- Miralles, D.G., Teuling, A.J., van Heerwaarden, C.C., de Arellano, J.V.-G., 2014. Mega-heatwave temperatures due to combined soil desiccation and atmospheric heat accumulation. *Nat. Geosci.* 7, 345–349.
- Mishra, V., Ganguly, A.R., Nijssen, B., Lettenmaier, D.P., 2015. Changes in observed climate extremes in global urban areas. *Environ. Res. Lett.* 10, 024005.
- Mlawer, E.J., Taubman, S.J., Brown, P.D., Iacono, M.J., Clough, S.A., 1997. Radiative transfer for inhomogeneous atmospheres: RRTM, a validated correlated-k model for the longwave. *J. Geophys. Res. Atmos.* 102, 16663–16682.
- Nitta, T., 1987. Convective activities in the tropical western Pacific and their impact on the Northern Hemisphere summer circulation. *J. Meteorol. Soc. Jpn.* 65, 373–390.
- Noh, E., Kim, J., Jun, S.-Y., Cha, D.-H., Park, M.-S., Kim, J.-H., Kim, H.-G., 2021. The role of the Pacific-Japan pattern in extreme heatwaves over Korea and Japan. *Geophys. Res. Lett.* 48, e2021GL093990.
- Park, K., Baik, J.-J., Jin, H.-G., Tabassum, A., 2024. Changes in urban heat island intensity with background temperature and humidity and their associations with near-surface thermodynamic processes. *Urban Clim.* 58, 102191.
- Park, K., Jin, H.-G., Baik, J.-J., 2023. Contrasting interactions between urban heat islands and heat waves in Seoul, South Korea, and their associations with synoptic patterns. *Urban Clim.* 49, 101524.
- Possega, M., Aragão, L., Ruggieri, P., Santo, M.A., Di Sabatino, S., 2022. Observational evidence of intensified nocturnal urban heat island during heatwaves in European cities. *Environ. Res. Lett.* 17, 124013.
- Pyrgiou, A., Hadjinicolaou, P., Santamouris, M., 2020. Urban-rural moisture contrast: regulator of the urban heat island and heatwaves' synergy over a mediterranean city. *Environ. Res.* 182, 109102.
- Ramamurthy, P., González, J., Ortiz, L., Arend, M., Moshary, F., 2017. Impact of heatwave on a megacity: an observational analysis of New York City during July 2016. *Environ. Res. Lett.* 12, 054011.
- Ryu, Y.-H., Baik, J.-J., 2013. Daytime local circulations and their interactions in the Seoul metropolitan area. *J. Appl. Meteorol. Climatol.* 52, 784–801.
- Ryu, Y.-H., Baik, J.-J., Lee, S.-H., 2011. A new single-layer urban canopy model for use in mesoscale atmospheric models. *J. Appl. Meteorol. Climatol.* 50, 1773–1794.
- Salamanca, F., Kröp, A., Martilli, A., Clappier, A., 2010. A new building energy model coupled with an urban canopy parameterization for urban climate simulations—part I: formulation, verification, and sensitivity analysis of the model. *Theor. Appl. Climatol.* 99, 331–344.
- Skamarock, W.C., Klemp, J.B., Dudhia, J., Gill, D.O., Liu, Z., Berner, J., Wang, W., Powers, J.G., Duda, M.G., Barker, D.M., Huang, X.-Y., 2019. A Description of the Advanced Research WRF Model Version 4. NCAR Tech. Note TN-556+STR.
- Sun, T., Kottaus, S., Li, D., Ward, H.C., Gao, Z., Ni, G.-H., Grimmond, C.S.B., 2017. Attribution and mitigation of heat wave-induced urban heat storage change. *Environ. Res. Lett.* 12, 114007.
- Syed Mahbar, S.F., Kusaka, H., 2024. Synergistic interactions between urban heat islands and heat waves in the Greater Kuala Lumpur and surrounding areas. *Int. J. Climatol.* 44, 4886–4906.

- Takaya, K., Nakamura, H., 2001. A formulation of a phase-independent wave-activity flux for stationary and migratory quasigeostrophic eddies on a zonally varying basic flow. *J. Atmos. Sci.* 58, 608–627.
- Tseng, K.-C., Ho, Y.-H., 2024. The subseasonal predictability of the western North Pacific subtropical high and the 2020 record-breaking event. *npj Clim. Atmos. Sci.* 7, 53.
- Tuholske, C., Taylor, K., Funk, C., Verdin, A., Sweeney, S., Grace, K., Peterson, P., Evans, T., 2021. Global urban population exposure to extreme heat. *Proc. Natl. Acad. Sci. U.S.A.* 118, e2024792118.
- Varentsov, M., Konstantinov, P., Repina, I., Artamonov, A., Pechkin, A., Soromotin, A., Esau, I., Baklanov, A., 2023. Observations of the urban boundary layer in a cold climate city. *Urban Clim.* 47, 101351.
- Wang, L., Li, D., 2019. Modulation of the urban boundary-layer heat budget by a heatwave. *Q. J. R. Meteorol. Soc.* 145, 1814–1831.
- Wu, Y., Zhao, K., Huang, J., Arend, M., Gross, B., Moshary, F., 2019. Observation of heat wave effects on the urban air quality and PBL in New York City area. *Atmos. Environ.* 218, 117024.
- Xin, J., Zhang, Y., Bai, W., Song, Z., 2024. Response of urban heat island effects within the planetary boundary layer to heat waves and impact of horizontal advection over Shanghai. *Atmos. Res.* 311, 107721.
- Yang, Q., Xu, Y., Chakraborty, T.C., Du, M., Hu, T., Zhang, L., Liu, Y., Yao, R., Yang, J., Chen, S., Xiao, C., Liu, R., Zhang, M., Chen, R., 2024. A global urban heat island intensity dataset: generation, comparison, and analysis. *Remote Sens. Environ.* 312, 114343.
- Zhang, Y., Wang, L., Santanello Jr, J.A., Pan, Z., Gao, Z., Li, D., 2020. Aircraft observed diurnal variations of the planetary boundary layer under heat waves. *Atmos. Res.* 235, 104801.
- Zhao, L., Oppenheimer, M., Zhu, Q., Baldwin, J.W., Ebi, K.L., Bou-Zeid, E., Guan, K., Liu, X., 2018. Interactions between urban heat islands and heat waves. *Environ. Res. Lett.* 13, 034003.
- Zhao, Y., Zhong, L., Zhou, K., Liu, B., Shu, X., 2024. Responses of the urban atmospheric thermal environment to two distinct heat waves and their changes with future urban expansion in a Chinese megacity. *Geophys. Res. Lett.* 51, e2024GL109018.
- Zong, L., Liu, S., Yang, Y., Ren, G., Yu, M., Zhang, Y., Li, Y., 2021. Synergistic influence of local climate zones and wind speeds on the urban heat island and heat waves in the megacity of Beijing, China. *Front. Earth Sci.* 9, 673786.